Geochemical detection of shallow mantle fluid along the San Andreas Fault

by

Victoria Rebecca Balkwill Tweedie

Department of Earth & Planetary Sciences

McGill University

Montreal, Quebec, Canada

October, 2017

Submitted to McGill University in partial fulfillment of the requirements of the degree Master of Science

Abstract

The San Andreas Fault (SAF) is an earthquake hazard to millions of people living proximal to the fault system in California. Fluids drive movement and cause stress redistribution along the SAF but their origin and subsurface migration are not well understood. Helium isotopic evidence suggests some mantle fluid contribution to the fault near Parkfield and in southern California south of the Big Bend but previous studies have been unsuccessful in detecting these signatures in the shallow fault system.

Isotopic measurements ($\delta^{13}C$) of soil CO_2 gas were collected along transects perpendicular to the fault in San Benito County, Parkfield, and the Carrizo Plain, and analyzed using a portable cavity ring down-spectrometer (CRDS). The high precision measurements were analyzed with Keeling plots, revealing representative $\delta^{13}C$ signatures for each transect ($\delta^{13}C_Y$). Literature values were used to establish end-member $\delta^{13}C$ signatures for biogenic ecosystem CO_2 ($\delta^{13}C_R$) and mantle CO_2 ($\delta^{13}C_M$). The proportion of $\delta^{13}C_R$ and $\delta^{13}C_M$ required to yield each transect's $\delta^{13}C_Y$ signature was then computed and used to determine the flux of mantle CO_2 (M_f) to the system. These results were compared with ^{222}Rn measurements gathered from four of the seven transects. Biogenic ecosystem respiration was unable to account for the signatures observed in seven transects, revealing that mantle fluids are present and detectable in the shallow fault system. Mantle proportions and fluxes present in the transects reveal enrichment from north (0 %) to south (38.16 %). Findings are supported by enhanced ^{222}Rn concentrations in the south revealing enhanced permeability in the Carrizo Plain. These findings do not reflect geochemical differences between creeping and locked segments of the fault; they may reflect how the interaction of the Big Bend and the Garlock-Big Pine fault system near the Carrizo Plain influences fluid migration and stress accumulation.

Résumé

La faille San Andreas (FSA) est un danger de tremblement de terre pour des millions de gens vivant à proximité de la faille en Californie. Les fluides entraînent le mouvement et provoquent une redistribution du stress le long de la FSA mais leur origine et migration sous-sol n'est pas bien comprise. Les preuves isotopiques d'hélium suggèrent une contribution fluide du manteau à la faille près de Parkfield et dans le sud de la Californie au sud du Big Bend mais des études antérieures ont échoué à détecter ces signatures dans le système de faille peu profonde.

Les mesures isotopiques ($\delta^{13}C$) des gaz de CO_2 du sol ont été recueillies le long des transects perpendiculaires à la faille dans le Comté de San Benito, Parkfield et la Plaine Carrizo, et ont été analysées à l'aide d'un spectromètre de cavite anneau-bas (SCAB). Les mesures de haute précision ont été analysées avec des parcelles de Keeling, révélant des signatures $\delta^{13}C$ représentatives pour chaque transect ($\delta^{13}C_Y$). Les valeurs de la littérature ont été utilisées pour établir les signatures $\delta^{13}C$ des membres finaux pour l'écosystème biogène CO_2 ($\delta^{13}C_R$) et le CO_2 du manteau ($\delta^{13}C_M$). La proportion de $\delta^{13}C_R$ et $\delta^{13}C_M$ requis pour produire la signature $\delta^{13}C_Y$ de chaque transect a ensuite été calculée et utilisée pour determiner le flux de CO2 de la manteaux (Mf) dans le système. La respiration de l'écosystème biogénique était incapable de tenir compte des signatures observées dans sept transects, révélant que les fluides du manteau sont présents et détectables dans le système de faille peu profonde. Les proportions de manteau présentes dans les transects révèlent un enrichissement du nord (0 %) vers le sud (38.16 %). Les résultats sont soutenus par des concentrations accrues de ^{222}Rn dans le sud révélant une perméabilité accrue dans la Plaine Carrizo. Ces résultats ne reflètent pas les differences géochimique entre les segments rampants et verrouillés de la faille; il peut refléter comment l'interaction du Big Bend et du système de failles Garlock-Big Pine près de la Plaine Carrizo influence la migration des fluides et l'accumulation du stress.

Preface

The following thesis presents original research by the author at the Department of Earth and Planetary Sciences at McGill University during 2015 to 2017. This work is presented as one article intended for submission to a peer-review journal of which the author is the main contributor and John Stix is the co-author. Field work, sample preparation, data collection, and analyses were conducted by the author under the supervision of John Stix.

Acknowledgements

I would first like to thank my supervisor Professor John Stix for his continued support and guidance through my time at McGill University. Thank you to my committee member Professor Christie Rowe for providing guidance and insight into structural geology. I would I also like to thank Diane Hanano and all of the MAGNET researchers and trainees for providing me with invaluable opportunities to grow as a geochemist. I would like to thank my parents, my sister, and my partner for their unwavering love and support throughout my Masters degree.

I am most grateful to several key individuals who helped make this research possible. Jon Erskine of Graniterock helped us select an appropriate location for our transect SB-GR and provided us access to GraniteRock property. Discussions with Jon Erskine, Emily Brodsky, and Lian Xue (UC Santa Cruz) were very useful and enlightening for our work. Scott Soares of the Hollister Hills State Vehicular Recreation Area helped us to acquire permission to sample, select an appropriate location, and assisted us with some data collection along transect SB-HH. Tony DeRose of DeRose Vineyards granted us permission to perform a transect at the vineyard. Andy Snyder of the U.S. Geological Survey showed us key boreholes and wells to sample, and also provided us access to our soil survey site near Parkfield. Denis Kearns of the Bureau of Land Management provided permission to sample along the fault in the Carrizo Plain. I thank all the landowners for their gracious permission to access their lands so that we might study the fault.

Finally, I would like to thank my Magma Chamber mates at McGill: Fiona D'Arcy, Clara Waelkens, Charlie Beard, Shane Rooyakkers, and Lynsday Moore for their friendship and enthusiasm for volcanology over the past two years.

Table of Contents

List of Figures

List of Tables

Chapter One: General Introduction

The San Andreas Fault (SAF) is a right-lateral strike-slip fault that extends 1100 km through the state of California. The SAF formed around 30 Ma at the boundary between the Pacific and North American Plates, following a shift from subduction to transform motion and the development of the Mendocino Triple Junction (Wallace, 1990). At present, the SAF is one of the most studied fault systems in the world. This is because nearly 30 million people live close to the SAF and our current knowledge of the system makes forecasting catastrophic earthquakes uncertain. According to the geologic record, catastrophic earthquakes (>M 7.5) near the Carrizo Plain in southern California occur every ~100 years (U.S. Geological Survey, 2008). The most recent occurred 160 years ago in 1857 (M 7.9 Fort Tejon) making this region overdue for an earthquake. The USGS forecasts the southern SAF has a 16% chance of experiencing an earthquake of M 7.5 or greater in the next 30 years. While the prediction of large earthquakes along the SAF is currently impossible, the Parkfield area experiences regular earthquakes (M 6.0) on average every 22 years (12-30 years). Parkfield is located near the southern extent of the creeping segment of the central SAF (Figure 1). The earthquakes at Parkfield are smaller and more predictable than those in the locked segments of the fault because the fault's creeping movement is thought to enable pressure and fluids in the subsurface to be redistributed, preventing the buildup of large quantities of stress, which would cause catastrophic earthquakes.

The SAF near Parkfield is comprised of two principal geologic terranes, the Salinian Block and the Franciscan complex, representing the North American and Pacific plates, respectively. These geologic units have experienced immense displacement and deformation from subduction and transform motion. The Salinian Block is mainly comprised of granitic plutonic rocks, while the Franciscan complex represents oceanic lithosphere, which has been accreted onto the North American plate and is comprised of weakly metamorphosed accretionary prism deposits (Unsworth et al., 1998). North near San Juan Bautista the western side of the fault is comprised of the Franciscan complex while the east is made up of marine sedimentary rocks of the Great Valley Sequence overlain by thick Cenozoic sediments. The western Caliente and the eastern Temblor mountain ranges surround the southern Carrizo Plain. The Caliente mountain range is underlain by Precambian marine and terrestrial deposits containing some Tertiary basalts

(Jennings and Strand, 1969), while the marine sediments of the Monterey Formation underlie the Temblor mountain range.

In order to make accurate hazard forecasts for this system it is imperative to understand the processes that combine to produce these hazards. Earthquake activity at the SAF is driven by elevated pore fluid pressure, which reduces the rock's effective stresses (Rice, 1992). The origin of the fluids driving fault movement and seismic activity at the SAF has been a topic of debate in the literature. In 1990 Byerlee showed that fluids originating strictly from the crust can explain near lithostatic pore pressures in the SAF. However, in 1992 Rice et al. proposed that these fluids originate from mantle or deep crustal sources, as the movement of fluids through the ductile root of the fault would enable pore fluid pressure to rise above the overburden pressure, resulting in fault rupture and seismic activity. The distinction between fluid source(s) is important because it permits greater understanding of fault properties and fluid migration within the system. Magnetotelluric (MT) studies have found low resistivity regions proximal to the fault extending to depths of 30 to 50 km (Becken et al., 2008). MT studies show very low resistivity zones near shallow depths in the fault zone, which is not surprising as faults are believed to contain flower structures radiating from depth to the surface of the fault trace (Unsworth et al., 1997). These structures allow the creation of low resistivity zones at depth by the collection of fluids.

In 1997 Kennedy et al. measured helium ratios ($^3He/^4He$) in well waters proximal to the SAF system, discovering elevated quantities of mantle helium in the Varian-Phillips well (2.0 R_A) near Parkfield and Mercy Hot Springs (4.0 R_A) 50 km southwest of Hollister, where R_A is the $^3He/^4He$ ratio corrected to the atmosphere. On Earth, ^3He originates from the mantle where it was entrapped during the planet's formation and ^4He is a radioactive decay product present in the crust. ^3He is also present in the Earth's atmosphere, which is why it is important to correct for atmospheric influences. Helium samples from the main hole of the San Andreas Fault Observatory at Depth (SAFOD) identified somewhat greater quantities of mantle helium in the North American Plate (0.9 R_A, ~11%) than the Pacific Plate (0.4 R_A, ~5%) (Wiersberg and Erzinger, 2007). CO_2, a large and immiscible molecule in the mantle is known to transport smaller helium molecules from the mantle into the crust. As a result the geochemical analysis of CO_2 isotopes and concentrations should provide information into fluid movement in the fault system. While previous work has identified mantle-derived helium present in deep wells (Kennedy et al., 1997), the geochemical detection of shallow mantle signatures in the fault system, by soil gas analysis, has not been successful. Previous work by Lewicki and Brantley (2000) and Lewicki et al. (2003) measured stable isotopes of soil CO_2 near Hollister on the Calaveras fault and near Parkfield on the SAF, with $\delta^{13}C$ signatures ranging between -23.7 ‰ and -16.4 ‰. The authors concluded that these values merely reflect biogenic signatures at such shallow depths between 10 cm and 80 cm. If mantle fluids are present in the shallow fault system, they likely exist in small quantities, requiring more sensitive mixing analyses.

In this thesis soil CO_2 gases were collected from the northern locked, central creeping, and southern locked segments of the SAF. Analysis of CO_2 was performed by a Picarro G1101-i cavity ring-down spectrometer (CRDS) to analyze CO_2 concentration and $\delta^{13}C$ in order to detect small mantle CO_2 contributions to the fault system along different segments of the SAF. These data are combined with well samples collected and analyzed by the author and previous studies (Lewicki and Brantley, 2000 and Lewicki et al., 2003) to compare the mantle CO_2 contributions in different structural regions of the fault system. CO_2 flux and ^{222}Rn data collected during the course of this thesis are presented in Appendix A at the end of this thesis. CO_2 flux data provides insight into the rate of CO_2 migration and production in the soil. ^{222}Rn is a radioactive decay product of the Uranium-238 and Radon-226 decay chain. ^{222}Rn has a short half-life of 3.8 days and has been used in active fault zone around the world in order to understand fluid migration and permeability.

Chapter Two: Detection of Mantle CO_2 along the San Andreas Fault, California

Victoria Tweedie[1], John Stix[1]

[1] Department of Earth and Planetary Sciences, McGill University, 3450 University Street, Montreal, Quebec H3A 0E8, Canada.

Abstract

An increasing body of evidence suggests that fluids originating from the Earth's mantle drive fault movement and earthquake activity along the San Andreas Fault (SAF). Mantle helium, which has been found in varying quantities along the SAF, is likely transported from the mantle by CO_2 molecules, however studies have failed to recognize mantle signatures in CO_2 in the SAF system. In this study we measured soil CO_2 gas along the SAF between San Juan Bautista and the Carrizo Plain in California, focusing on three regions of interest (i) locked to transitional San Benito County, (ii) creeping to transitional Parkfield, and (iii) the locked Carrizo Plain. Three fault-perpendicular transects were analyzed in April 2016 and four in November 2016. CO_2 flux and ^{222}Rn were measured along four of the seven transects to understand soil gases and permeability in each region. δ^{13}C from CO_2 was measured by a portable cavity ring-down spectrometer (CRDS), and subsequently analyzed by Keeling plots and mixing proportions. Analyses reveal (i) CRDS yields high precision δ^{13}C measurements in fault zones, (ii) mantle CO_2 is detectable in the shallow fault system, and (iii) mantle CO_2 contributions are enriched in the shallow fault system from north to south. These findings show that sensitive analyses are required for the detection of deeply degassing CO_2 and that tectonic forces from the Big Bend segment of the SAF may play a more important role in deep fluid migration at the Carrizo Plain and more northern parts of the SAF than previously thought.

2.1 Introduction

High pore fluid pressure has long thought to drive fault creep along the San Andreas Fault (SAF) (e.g., Irwin and Barnes, 1975); however, the origin or origins of these fluids is a topic of considerable debate. The two prevailing models rely on fault-weakening fluids originating from strictly crustal sources such as meteoric waters or serpentinite (Byerlee, 1990; 1992) or deep crustal or mantle sources (Rice, 1992). Helium isotopic rations ($^3He/^4He$) from drill-mud at San Andreas Fault Observatory at Depth (SAFOD) (Weirsberg & Erzinger, 2007) and from wells along the SAF near Parkfield and the Salton Sea (Evans et al., 2013; Kennedy et al., 1997) provide evidence for a contribution from mantle fluids along the SAF. ^3He, which originates from the Earth's mantle is likely carried from depth by larger, incompatible CO_2 molecules (e.g., Hauri et al., 2002). However, while previous studies of soil CO_2 have discovered anomalously high CO_2 fluxes proximal to the SAF (Lewicki and Brantley, 2000), they observed $\delta^{13}C$ signatures between -23.7 ‰ and -16.4 ‰. These signatures fall within $\delta^{13}C$ ranges for C3 (-37 ‰ to -20 ‰; Kohn, 2010) and C4 (-16 ‰ to -10 ‰; O'Leary, 1988) vegetation. As a result the soil gases were classified as strictly biogenic in origin with no contribution from the mantle (-9 ‰ to -4 ‰; Pineau and Javoy, 1983). However, these studies do not account for small inputs of deep mantle CO_2, which would be difficult to detect when diluted with high quantities of biogenic $\delta^{13}C$ signatures in the shallow fault system.

The primary objectives of this study are to establish whether (i) deep CO_2 is present and detectable in the shallow fault system, and (ii) there exist geochemical differences in CO_2 isotopes and concentrations between creeping and locked segments of the fault.

To establish whether deep mantle CO_2 is present in the shallow fault system, we measured carbon isotopes ($\delta^{13}C$) and CO_2 concentrations from soil gas at seven transects across the fault in three regions of California: San Benito County, Parkfield, and the Carrizo Plain (Figure 1). CO_2 flux and ^{222}Rn concentrations were measured along 4 of the 7 transects to enhance interpretation of soil gas results. ^{222}Rn, a product of the radioactive Uranimum-238 decay chain with a short half-life of 3.8 days, was measured as an independent marker of permeability along the fault zone. ^{222}Rn is used around the world as an indicator of fault and geologic permeability (e.g., Nikolopoulos et al., 2015).

Fault sections at Parkfield and southern San Benito County are considered creeping to transitional, while those of northern San Benito County and Carrizo Plain are locked. Where locked segments of the SAF undergo no strike-slip displacement annual and creeping segments experience the greatest quantities of aseismic fault slip. Transitional areas represent a shift from locked to creeping motion, however the annual aseismic slip in these regions is less than in creeping segments. The SAF at San Benito County transitions quickly from locked (0.1 mm/yr) to creeping (11.7 mm/yr) motion from north to south of San Juan Bautista (San Benito County, 2010). The last major earthquake near this region was the October 17, 1989, Loma Prieta earthquake (magnitude 6.9) near the Santa Cruz Mountains. Parkfield represents a transition from northern creeping to southern locked motion with a fault creep rate of 9.3 mm/yr (Titus et al., 2006). This region is well known for recurring magnitude 6.0 earthquakes on approximately 22-year cycles, with the most recent occurring in 2004. The Parkfield section of the fault is highly fractured and seismicity may be due to high pore fluid (Unsworth et al., 1997). The Carrizo Plain encompasses the southern locked segment of the SAF where the last large earthquake in this region was the magnitude 8.3 Fort Tejon earthquake of January 9, 1857, after which time it has remained locked without aseismic creep, unlike at Parkfield and San Benito County.

2.2 Field and analytical methods

Two field campaigns were conducted, one in April 2016 and a second in November 2016, to make geochemical measurements of soil CO_2 gas, ^{222}Rn, and CO_2 efflux along fault-perpendicular transects in California. In April 2016 we surveyed three 6-station transects, one in Parkfield (PK-1) and two in the Carrizo Plain (CP-1, CP-2). In November 2016 we measured three transects in San Benito County (SB-GR, SB-HH, SB-DV) and one in the Carrizo Plain (CP-3), however ^{222}Rn and CO_2 flux measurements were only made along CP-3. In April we measured 6 stations for each transect, while in November we densified the array by measuring 11-13 stations for each transect. In April gas samples were also collected from water wells in Parkfield (8) and San Benito County (10).

2.2.1 Soil and well gas

Soil gases were pumped into sample bags from depths of 20 cm to 60 cm through a titanium soil probe using a Crowcon Triple Plus+ portable gas detector. The detector senses the presence of CO_2, H_2S, and H_2 gas. Well gases were collected from depths between 4 and 50 m using 1/8” diameter Tygon® tubing with small fishing weights attached to the lowest 1 m to ensure the tubing did not coil at the end. Sample bags were each flushed and filled twice before a final fill for geochemical analysis. Atmospheric CO_2 samples also were collected into sample bags with the pump positioned on the ground. We stood downwind several meters from the instrument to avoid contamination.

The gases were analyzed for concentrations of CO_2, CH_4, and H_2O in addition $\delta^{13}C$ of CO_2 each evening using a Picarro G1101-i cavity ring-down spectrometer (CRDS). Although the instrument's quoted precision is ±0.5‰ for $\delta^{13}C$, Lucic et al. (2015) found the precision to be slightly concentration dependent with variations up to 0.6‰ between 500 and 5000 ppm. In order to reduce this effect, gas samples and standards were analyzed at similar concentrations around 1500 ppm CO_2 by dilution with scrubbed air when possible. A copper tube filled with copper filings was connected between the instrument and the collection bags to remove any potential H_2S interference (Malowany et al., 2015). A 1 μm Acrodisc CR 25 mm syringe filter was placed before the collection bags to remove any particulate matter. Each sample was measured for at least 10 minutes (10 s frequency), and an average value over this time period was recorded for CO_2 (ppm), the raw $\delta^{13}C$ value relative to ‰ V-PDB, H_2O (wt %), and CH_4 (ppm).

The instrument's isotopic measurements were calibrated using three CO_2 standards with different $\delta^{13}C$ signatures (-43.0, -15.3, and -11.4 ‰) to ensure optimal accuracy. Two replicates of each standard were prepared at concentrations of ~1500 ppm, which is comparable to sample concentrations. The average $\delta^{13}C$ value of each replicate acquired from the instrument over the 10-minute period was plotted against the standard's known $\delta^{13}C$ signature. Sample and standard precision was monitored through the variation in $\delta^{13}C$ signatures recorded over the minimum 10-minute period.

A linear best-fit equation was generated and used to calibrate the instrument for sample measurements. Measurement of the CO_2 standard of -15.60 ‰ run with samples varied from -16.26 to -14.73 $\pm$ 0.42 ‰ (avg. -15.29‰) in April and -16.01 to -14.74 $\pm$ 0.42 ‰ (avg. -15.37‰) in November. Little $\delta^{13}C$ variation was observed in standards over the course of a run in April (0.03 to 0.60 ‰;) while in November slightly larger variations were observed (0.42 to 1.13 ‰).

Analytical errors in CO_2 concentrations may have arisen from sample and standard dilutions for gas analysis. Standards and the samples with field-measured CO_2 concentrations greater than 1500 ppm were diluted with scrubbed air by an electrical pump. An appropriate flow rate was selected to achieve the desired volume over a select time period. However, the flow rate was sometimes prone to deviations, slightly altering the concentration of CO_2 in different samples and standards.

2.2.2 Radon concentrations

Radon (^{222}Rn) was measured using E-PERM® electrets buried in the soil. E-PERM® electrets contain a Teflon disk which is electrically charged. Nuclear radiation emitted during the decay of radon generates ions. These ions are attracted to the electrostatic field produced by the charged electret. Only radon gas is permitted to diffuse through the electret chamber. Upon capture of ions emitted from radon, the surface charge of the electret decreases.

Two electrets, one low-sensitivity (long-term) E-Perm electret in a L-chamber and one high-sensitivity (short-term) E-Perm electret in a M-chamber, were placed in a hole at 20-30 cm depth at locations in Parkfield and the Carrizo Plain where soil gas was measured. To limit condensation effects the electrets were covered with a 950 mL cylindrical plastic container just prior to burial in the soil for 2-5 days. The voltages of the electrets were measured twice, an initial reading (I) prior to exposure and a final reading (F) following the exposure. Using the difference in voltage (I – F) and the exposure time (D), the information was converted to quantity of ^{222}Rn using experimentally derived corrections for the chamber and electret combination. Corrections for gamma radiation and elevation were made to calculate accurate radon measurements in pCl/L. Electrets that had dirt on the Teflon disk were considered contaminated and the results were not used.

2.2.3 CO_2 flux

CO_2 flux was measured using a LICOR LI-8100A Automated Soil Gas Flux System by the chamber accumulation method (e.g. Sorey et al., 1998). Cylindrical soil collars were hammered 4-10 cm into the soil and the soil was allowed to adjust to the disturbance of collar-insertion for at least 18 hours. At each station there was a 30-second dead band accumulation followed by five 2-minute CO_2 flux measurements with a 90-second post purge period between each measurement. The LI-8100A computes the CO_2 flux (F_c) from the soil as

$$F_c = \frac{10CP_0(1 - \frac{W_0}{1000})}{RS(T_0 + 273.15)} \frac{\partial C'}{\partial t}$$

where F_c is the soil CO_2 flux (µmol m^{-2} s^{-1}), V is the volume (cm^3), P_0 is the initial pressure (kPa), W_0 is the initial mole fraction of water vapour (mmol mol^{-1}), S is the soil surface area (cm^2), T_0 is initial air temperature (°C), and $\partial C'/\partial t$ is the initial rate of change in water-corrected (dry) CO_2 mole fraction (µmol mol^{-1}) (LI-COR Biosciences Inc., 2012). The first measurement at each station returned highly variable values and was excluded from further calculations at each station. The final four of five CO_2 flux measurements were combined to generate an average CO_2 flux for each transect.

2.3 Results

2.3.1 Atmospheric CO_2

The atmospheric CO_2 measurements range from 399 ppm to 409 ppm. Global atmospheric CO_2 in 2016 averaged 403 ppm, and varied seasonally between 403 and 407 ppm, in November and April, respectively (Scripps/NOAA, Mauna Loa CO_2; 2016, www.co2now.org). Measurements with CO_2 greater than 410 ppm were discarded as they were considered contaminated by other sources such as petroleum emissions or biogenic respiration. Atmospheric $\delta^{13}C$ signatures range from -7.64 to -6.17 $\pm$ 0.49 ‰. We did not observe atmospheric $\delta^{13}C$ variation seasonally or over the course the day in April or November.

2.3.2 Soil gas CO_2

A total of 71 soil gas measurements of $\delta^{13}C$ (-29.72 to -9.28 ‰) and CO_2 (427 to 25,220 ppm) were collected (Table 1). The transect SB-GR has the most depleted and wide array of $\delta^{13}C$ signatures (-29.09 to -19.39 ‰, avg. -26.62 ‰). The other transects located in San Benito County (SB-HH: -24.88 to -17.45 ‰, avg. -21.58 ‰; SB-DV: -23.80 to – 19.11 ‰, avg. -21.02 ‰) and in Parkfield (PK-1: -22.26 to -18.68 ‰, avg. -21.01 ‰) have $\delta^{13}C$ signatures that are more enriched than SB-GR. Isotopic signatures from the Carrizo Plain are more enriched than the other three regions, which may in part be due to the region's aridity. Vegetation in arid regions, with higher temperatures and less available H_2O, conserve energy in this harsh climate by reducing CO_2 fractionation during photosynthesis resulting in more enriched $\delta^{13}C$ signatures than vegetation in more temperate regions. Transect CP-3 (-12.59 to -9.28 ‰, avg. -10.81 ‰) is significantly more enriched than CP-1 (-17.97 to -15.28 ‰, avg. -16.69 ‰) and CP-2 (-16.91 to -15.72 ‰, avg. 16.21 ‰).

High CO_2 was measured at the most northern transects: SB-GR (1032 to 25220 ppm, avg. 11221 ppm) and SB-HH (808 to 13180 ppm, avg. 4187 ppm). Soil CO_2 concentrations decrease towards SB-DV (1169 to 4717 ppm, avg. 2348 ppm) and PK-1 (1695 to 3920 ppm, avg. 2863). The lowest CO_2 concentrations are found in the Carrizo Plain (CP1: 1246 to 1802 ppm, avg. 1538 ppm; CP-2: 1352 to 1718 ppm, avg. 1457 ppm; CP-3: 427 to 522 ppm, avg. 477 ppm). CO_2 concentrations measured in November (CP-3) are notably lower than those from April (CP-1, CP-2).

2.3.3 Well gas CO_2

19 well gas samples were collected from 6 wells in Parkfield and 7 wells in San Benito County with great variation in CO_2 (121 to 182353 ppm) and $\delta^{13}C$ (-34.22 to -10.55 ‰) signatures. Gases from wells DW-11 and WGH have much greater CO_2 concentrations (182353 ppm and 11805 ppm, respectively) compared to other wells in San Benito County (759 to 37590 ppm) and Parkfield (824 to 1615 ppm) (Table 2).

2.3.4 CO_2 flux

30 CO_2 flux measurements were made along 4 of the 7 transects (CP-1, CP-2, CP-3, and PK-1). The CO_2 flux measurements range from 0.43 μmol $m^{-2}s^{-1}$ at CP-2 to 1.37 μmol $m^{-2}s^{-1}$ at PK-1. We observe great variation in CO_2 flux measurements collected at CP-3, which we attribute to being closely tied to the time of day (Figure 2). We observe that measurements made earlier in the morning had much lower CO_2 flux measurements than those made in the previous afternoon. As a result these CO_2 flux data for CP-3 was discarded as it is not reliable for comparisons with the other 3 transects. The average CO_2 flux at Parkfield (PK-1: 1.08 μmol $m^{-2}s^{-1}$) is greater than in the Carrizo Plain (CP-1: 0.97 μmol $m^{-2}s^{-1}$; CP-2: 0.79 μmol $m^{-2}s^{-1}$). Greater CO_2 flux at Parkfield may reflect greater photosynthetic activity relative to the arid Carrizo Plain.

2.3.5 Radon-222 Concentrations

60 ^{222}Rn concentration measurements (30 short-term electrets and 30 long-term electrets) were made in 30 locations along 4 different transects in April (3) and November (1). Short- and long-term electrets from the same location provide similar ^{222}Rn measurements with the exception of a few outlier pairs (CP-1B, CP-2F, and PK-1E). Outlier pairs were included in further analyses as their values are not the result of human or experimental error (e.g., errors in electret deployment, retrieval or measurement), leaving no real reason for their exclusion. The median ^{222}Rn of each transect was calculated to avoid disproportional weighting of non-

representative outliers attained in the average. The ^{222}Rn values in the Carrizo Plain in April (CP-1: 346.6 pCi/L; CP-2: 369.8 pCi/L) and November (CP-3: 367.9 pCi/L) are greater than Parkfield (PK-1: 113.4 pCi/L). These results are unexpected due to similarities in soil type in all localities. Transects CP-2 and CP-3, which are found at the same location have similar ^{222}Rn concentrations, suggesting that ^{222}Rn experiences little seasonal variation.

2.4 Discussion

The CO_2 information presented in the results section provides interesting trends and anomalies between different regions sampled. In the following discussion we first establish $\delta^{13}C$ end-members for the atmosphere ($\delta^{13}C_A$), the biogenic ecosystem ($\delta^{13}C_R$), and the mantle ($\delta^{13}C_M$). We then construct Keeling plots for each transect, extracting the representative intercept ($\delta^{13}C_Y$). We analyze whether the intercepts are in fact representative of each region. Using the mantle and biogenic end-member, we look at mixing proportions required to yield the transect's signature ($\delta^{13}C_Y$), establishing whether biogenic respiration can fully account for the signatures observed. Finally, we use our geochemical findings to interpret processes influencing fluid migration along the SAF.

2.4.1 Atmospheric End-Member

The atmospheric end-member, $\delta^{13}C_A$, for each transect is defined by the atmospheric measurements that were made in that region group in this study. For example, atmospheric measurements from Hollister Hills and DeRose Vineyards are used as the atmospheric end-member from SB-GR, SB-HH, and SB-DV. This ensures that the atmospheric end-member for each transect is closely related in space and time. In April 2016 the global atmospheric average was 407.42 ppm while our measurements ranged from 399 to 405 ppm, which are lower than the values measured at the Mauna Loa observatory. In November 2016 the average measured at Mauna Loa was 403.53 ppm, while we measured 399 to 409 ppm in this study. Small variation was observed in $\delta^{13}C_A$ signatures measured in both April and November. Those measured in April averaged -6.98 ‰, ranging from -7.64 to -6.17 ‰, while those measured in November averaged -6.78 ‰, ranging from -7.18 to 6.45 ‰. Similarities in CO_2 concentrations and $\delta^{13}C_A$

signatures reveal similar atmospheric background influences on the soil gas measurements made during both seasons.

2.4.2 Biogenic Ecosystem End-Member

The biogenic ecosystem end-member, $\delta^{13}C_R$, is a combination of heterotrophic (microbial) and autotrophic (vegetation) respiration. Autotrophic $\delta^{13}C$ varies predominantly by photosynthetic pathway (C3 vs. C4). The $\delta^{13}C$ value of C3 vegetation is dependent largely on annual precipitation and altitude (Kohn, 2010); therefore, $\delta^{13}C$ for each of the three region groups was determined individually. We used $\delta^{13}C$ signatures from previous work with (i) average annual precipitation within 2 inches of each region and (ii) with an altitudes less than 1000 m to define a range of C3 heterotrophic respiration for each region (Table 3).

Buck-Diaz and Evens (2011) mapped the dominant vegetation types in the Carrizo Plain revealing the location and distribution of C3 and C4 vegetation, specifically *Atriplex polycarpa* ($\delta^{13}C$: -17.6‰; Smith and Epstein, 1971). Figure 3 shows strictly C3 vegetation surrounding transect CP-1, and some C4 vegetation surrounding transects CP-2 and CP-3. C4 vegetation comprises approximately 8 and 13% of all vegetation within a 10 m radius of CP-2 and CP-3, respectively. This proportion was used to mix the $\delta^{13}C$ signature of *A. polycarpa* with the more depleted C3 vegetation end member to yield a broader range of biogenic signatures along CP-2 and CP-3.

According to previous studies autotrophic $\delta^{13}C$ signatures are enriched from +1.7 ‰ (Bowling et al., 2008) to +4 ‰ (Cerling et al., 1991) relative to heterotrophic signatures. The measurement of +4 ‰ enrichment originates from a highly productive montane environment in California, a region which is more productive than those found in this study. Due to uncertainty in selecting an appropriate autotrophic enrichment value for the regions in this study, the depleted and enriched biogenic end-member were defined by +1.7 ‰ and +4.0 ‰, respectively (Table 4). The carbon isotopic signature of biogenic respiration ($\delta^{13}C_R$) in each region was then computed as 25% heterotrophic and 75% autotrophic respiration (Tu and Dawson, 2003).

The range of end-member $\delta^{13}C_R$ varies by region and by transect from -29.99 to -21.50 ‰ (Table 4). $\delta^{13}C_R$ becomes more enriched southward from San Benito County (-29.99 to -24.50 ‰), through Parkfield (-25.88 to -23.60 ‰), to the Carrizo Plain (-26.28 to -21.80 ‰), as the environments become drier. The $\delta^{13}C_R$ range is greater in the Carrizo Plain as it accounts for the possibility of 100% C3 vegetation and up to 13% C4 vegetation in the CP-2 transect.

2.4.3 Keeling Plots

Keeling plots permit interpretation of three end-member mixing, even when an end-member is present in small proportions. We created Keeling plots to interpret mixing between atmospheric, biogenic ecosystem, and mantle end-members for all transects and transect sections by plotting $\delta^{13}C$ against $1/CO_2$ for atmospheric and soil gas samples. The y-intercept of a linear trend-line through the plot provides $\delta^{13}C_Y$, the carbon isotopic signature for transects.

Keeling plot y-intercepts ($\partial^{13}C_Y$) for all transects, with the exception of CP-3, have high precision (R^2 = 0.93 to 0.99), showing that the samples are well represented by the linear trend. The measurement of low CO_2 concentrations by the CRDS for soil gas samples along transect CP-3 leads to greater error in $\delta^{13}C$ signatures, making these data unreliable for further interpretation (Table 1).

Soil gas samples from PK-1 (this study), collected in April, were compared to data from Lewicki and Brantley (2000) and Lewicki et al. (2003), which they collected between March and May 2000. This transect data is hereforth termed PK-L. PK-1 has an intercept of -24.08 ‰ and little vertical distribution reflected by a high R^2 value of 0.97. PK-L's intercept is -22.45 ‰ and has a fair amount of vertical distribution, likely reflecting the slightly lower degree of certainty (R^2: 0.95) in the Keeling plot intercept. Parkfield CO_2 concentrations in this study (PK-1; 1695 to 3920 ppm, avg. 2863 ppm) are much lower than PK-L (797 to 20900 ppm, avg. 9048 ppm) despite being measured during the same season. All points collected from PK-1 fall within the SAF fault zone. To better interpret these data we compared those that fell within the 500 m wide SAF fault zone at Parkfield (Unsworth et al., 1999) for PK-L (Figure 4f) and PK-1 (Figure 4d). Keeling plot intercepts from PK-1 (-24.08 ‰) and PK-L (-23.06 ‰) are close, however it is possible that differences in CO_2 and isotopic signatures between the two transects reflect temporal variations in the earthquake cycle. Data for PK-L was collected 4 years prior to the 2004 Parkfield earthquake (M 6.0) and 8 years after the 1992 Parkfield earthquake (M 4.7). It is possible that greater CO_2 and more depleted $\delta^{13}C$ signatures present in PK-L reflect fluid build up prior to the seismic event. In 2016, we are presumably a decade from another Parkfield earthquake and fluid contributions to the fault system are much lower. It is also possible that these differences may reflect climatic variations in $\delta^{13}C$ or respired CO_2.

Keeling plot intercepts for the Carrizo Plain (Figure 4g,h) are more enriched than those from Parkfield (Figure 4d) and San Benito County (Figure 4a,b,c). This trend is not surprising due to increasing aridity trending southwards but the magnitude of enrichment is noteworthy. The $\delta^{13}C_Y$ signature observed in the Carrizo Plain is dominantly biogenic CO_2 combined with some mantle CO_2, as the Keeling plot intercepts are just outside of the region's biogenic signature range. $\delta^{13}C_Y$ of the different transects deviate further from the enriched $\delta^{13}C_R$ end-members from north to south, demonstrating increasing mantle CO_2 contribution from north to south along the SAF.

2.4.4 End-Member Mixing Proportions and Fluxes

We assume that $\delta^{13}C_R$ and mantle CO_2 ($\delta^{13}C_M$) are the only two sources mixing to produce $\delta^{13}C_Y$. We can then compute the range of proportions that mantle CO_2 (p_M) contributes to each transect by:

$$p_M = \frac{(\delta^{13}C_Y - \delta^{13}C_R)}{(\delta^{13}C_M - \delta^{13}C_R)}$$

where the value for $\delta^{13}C_Y$ is static for each transect, while $\delta^{13}C_R$ and $\delta^{13}C_M$ alternate between the end-member minimum and maximum values (e.g., minimum $\delta^{13}C_M$ = -9 ‰, maximum $\delta^{13}C_M$ = -4 ‰; Table 4) to compute all possible combinations. The global minimum and maximum of p_M were then combined with average CO_2 flux measurements made along the four transects to yield relative rates of mantle fluid migration along transects in the Carrizo Plain and Parkfield (Table 4).

Uncertainties for all measurements were propagated through all calculations to determine the absolute uncertainty for p_M and mantle CO_2 flux (M_f) measurements. The p_M calculation uncertainties vary from 0.84 to 12.69 %, while M_f uncertainty values range from 0.09 to 0.13 μmol $m^{-2}s^{-1}$ (Table 4). While these uncertainties are large relative to p_M M_f values in Table 4 they are not larger than the highest p_M and M_f value revealing a very real possibility that there are mantle contributions to the SAF system at these locations and that these locations can be compared to one another in this respect in order to understand mantle fluid migration along the SAF in these regions. In fact, M_f uncertainties in Parkfield (PK-1: 0.12 μmol $m^{-2}s^{-1}$) are similar to those in the Carrizo Plain (CP-1: 0.11 μmol $m^{-2}s^{-1}$; CP-2: 0.13 μmol $m^{-2}s^{-1}$), despite great variation in M_f calculations (PK-1: 0.15 μmol $m^{-2}s^{-1}$; CP-1: 0.45 μmol $m^{-2}s^{-1}$; CP-2: 0.27 μmol $m^{-2}s^{-1}$).

SB-GR is the only transect that does not show any possibility of mantle influence due to its depleted soil CO_2 $\delta^{13}C$ signatures. It is unclear whether these signatures are a reflection of the transect's location in the northern locked segment or the more localized presence of grazing animals fertilizing the soil with depleted $\delta^{13}C$ signatures.

SB-GR also has the highest CO_2 measurements, despite being in a locked segment of the fault. Lewicki et al. (2003) also observed high CO_2 concentrations (21000 to 25200 ppm) in Hollister, San Benito County, at the Calaveras Fault just 15 km away. The western segment of SB-GR is underlain by a distinctive hornblende quartz gabbro sliver that has been highly fractured by the SAF (Ross, 1970). This sliver has also been offset over 160 km by the SAF. Gas samples from wells on this sliver along SB-GR (DW-11) and PK-1 (WGH) reveal greater CO_2 concentrations relative to surrounding wells. High fracture density in the block may channel CO_2 and other fluids to the surface, explaining the high CO_2 observed in this location. However, the depleted $\delta^{13}C$ raises additional questions about the origin of the CO_2. Similar to SB-HH and SB-DV, $\delta^{13}C$ signatures at the Calaveras Fault in Hollister are more enriched (-17.22 to -21.52 ‰; Lewicki et al., 2003) than seen at SB-GR. Surface vegetation and soil types at SB-GR and SB-HH are similar, suggesting that differences in subsurface geology may explain the differences in isotopic signatures. Anomalously high CO_2 and depleted $\delta^{13}C$ at SB-GR are likely due to fault and fractured rock trapping biogenic gas flow.

A large vertical array of $\delta^{13}C$ is seen in the SB-GR Keeling plot (Figure 4a). No obvious spatial trend is observed across the fault transect. It is possible that this vertical array reflects competing processes occurring along the transect. Perhaps a small component of mantle CO_2 enriches $\delta^{13}C$ signatures in soil fissures at some locations, while organic fertilizers, oil seeps or simply biogenic activity deplete the $\delta^{13}C$ signatures in other locations. However, since the transect signature as a whole is very depleted, it is unlikely that there is significant mantle CO_2 contribution to the regional budget.

For the other five transects these mixing proportions reveal that biogenic respiration in these environments is unable to account for the measured enrichment in $\delta^{13}C$ signatures. These signatures could be enriched by other sources, such as carbonates. Marine carbonates have enriched signatures ($\delta^{13}C$ ~ 0 ‰, Ohmoto and Rye, 1973), which could mix with $\delta^{13}C_R$ to generate enriched $\delta^{13}C_Y$ signatures. However, waters from wells and springs in Parkfield and the California oil fields near the Carrizo Plain show low carbonate alkalinity (Thordsen et al., 2010) suggesting that carbonates are unlikely to account for the enrichment in $\partial^{13}C_Y$ observed in these regions. These findings suggest that mantle CO_2 contributions to the shallow fault system are present.

In contrast, a large dolomite deposit is present in the valley where SB-HH and SB-DV are located, which may be a source of soil CO_2 enrichment (San Benito County, 1994). As a result, there exists some uncertainty whether the slight enrichment in $\partial^{13}C_Y$ for SB-HH and SB-DV are a result of mantle CO_2, crustal CO_2, or perhaps a combination of two.

The low mantle proportion (0 to 10.64 $\pm$ 8.29 %) and flux (0 to 0.15 $\pm$ 0.12 μmol $m^{-2}s^{-1}$), but greater CO_2 quantity measured at Parkfield shows greater CO_2 contributions from biogenic sources at shallow depths. Magnetotelluric (MT) data at Parkfield reveal high subsurface fluid content by means of low velocity zones (Becken et al., 2008). It is possible that this fluid, if originating from the mantle, is trapped within the subsurface geology and the fault zone, as we detect lower mantle contributions at the surface.

The Carrizo Plain has the lowest CO_2 and is most enriched in ^{13}C, which are a reflection of low respiration in the dry region. However, Keeling plot intercepts, mantle proportion, and mantle flux and for CP-1 (-20.16 ‰, 35.43 to 11.24 $\pm$ 12.69 %, 0.07 to 0.45 $\pm$ 0.11 μmol $m^{-2}s^{-1}$) and CP-2 (-19.68 ‰, 38.16 to 11.66 $\pm$ 10.49 %, 0.03 to 0.47 $\pm$ 0.13 μmol $m^{-2}s^{-1}$) reveal that biogenic respiration in this climate cannot fully explain these signatures. This suggests that mantle fluids do contribute to the shallow fault along these transects. The locked Carrizo Plain experiences limited seismic activity relative to the other two regions. Studies have found the fault zone in the Carrizo Plain to be narrow and low porosity, not highly fractured (Bedrosian et al., 2004), making this an unexpected location for mantle enrichment. MT studies reveal a low resistivity fault zone at the Carrizo Plain (Macke et al., 1997). The shallow conductive zone is comprised of Quaternary and Tertiary sediments as part of the Wells Ranch syncline, which are bound by the Morales thrust fault to the west and high resistivity crystalline rocks and another thrust fault to the east (Macke et al., 1997).

150 km south of the Carrizo Plain is the Big Bend segment, a 300 km section of the SAF that bends southeast, resulting from motion along the Garlock-Big Pine fault system. The left-

lateral Garlock fault intersects the SAF southeast of the Big Bend while the western Big Pine fault is a continuation of the Garlock fault, offset north by the SAF (Hill and Dibblee, 1953). Right-lateral motion along the SAF and the eastern orientation of the bend creates a compressional region resulting in crustal thickening. Compression is not possible without extension and crustal thinning in the regions surrounding the compression. Significant vertical thinning is observed along the Garlock fault 80 km south of the Carrizo Plain and the Rand Mountains 150 km to the east (Oldow and Cashman, 2009). Vertical thinning of the crust near the Carrizo Plain reduces the distance mantle fluids must travel to the surface.

Kulongoski et al. (2013) measured some of the highest $^3He/^4He$ ratios (0.10 to 3.52 R_A) proximal to the SAF in the Big Bend section. Just south of the Big Bend Evans (2013) observed mantle contributions decreasing from San Bernardino (1.73 R_A) to Coachella Valley (0.97 R_A) and then increasing south at the Salton Sea (2.23 R_A). Peak mantle fluid contributions at both San Bernardino and the Salton Sea are not surprising as they are both located in regions of extension and crustal thinning. San Bernadino is located in the Garlock fault's southern extensional zone and the Salton Sea is the most northern expression of the East Pacific Rise (Laznicka, 2010). However, mantle peaks in the Big Bend, a region of compression, may demonstrate high permeability, perhaps due to fractures or seismic activity, in this region under the influence of Garlock-Big Pine fault system.

2.4.5 ^{222}Rn Permeability

Soil gas and flux findings of mantle CO_2 in the Carrizo Plain are supported by elevated ^{222}Rn in the Carrizo Plain (CP-1: 346.6 pCi/L; CP-2: 369.8 pCi/L; CP-3: 367.9 pCi/L) relative to Parkfield (113.4 pCi/L). ^{222}Rn, originating from the decay of mantle Uranium and Thorium, is an independent marker of fault permeability due to its short half-life of 3.8 days. These findings are interesting as Parkfield is thought to be a highly fractured region of the fault with great permeability to fluid flow. It is possible that this study surveyed a low permeability region in Parkfield and that greater permeability regions exist nearby, such as localized near the hornblende quartz gabbro sliver mentioned previously or on the Pacific or North American plate. However, when compared with data from Lewicki and Brantley (2000) and Lewicki et al. (2003) that our data are not merely an instantaneous phenomena or an artifact of error propagation.

2.4.5 North to South Gradient

Mantle CO_2 contributions to the shallow fault system increase from north to south along the SAF as observed by ^{222}Rn, soil CO_2 concentrations, isotopes, and flux measurements. It is possible that the ascent of mantle fluids into the shallow Carrizo Plain are driven by high pore fluid pressure by southern stress accumulation compression and extension from the Garlock-Big Pine fault zone. It is uncertain whether these forces might influence fluid movement near Parkfield or in San Benito County as they are several hundred kilometers from the Big Bend. However, changes in subsurface fluid distribution and chemistry due to distant pressures such as earthquakes are common. Roeloffs (1998) found water levels in wells near Parkfield to change in response to earthquakes several hundred kilometers away. As a result it is possible that seismicity and stress redistribution in the Big Bend influence fluid migration in the Carrizo Plain and regions to the north.

2.5 Concluding Remarks

Mantle CO_2 is detectable in soil gases in the shallow fault system through analyses by Picarro G1101-i CRDS and Keeling plots. Biogenic end-members for each region were established from localities of comparable annual precipitation and altitude in the literature. Mantle contributions were found to increase from north (0%) to south (38%) along the SAF with fluxes increasing from 0.15 μmol $m^{-2}s^{-1}$ in Parkfield to 0.47 μmol $m^{-2}s^{-1}$ in the Carrizo Plain. Enhanced permeability and fluid migration is supported by high ^{222}Rn concentrations found in the Carrizo Plain (346.5 to 370.0 pCi/L) relative to Parkfield (113.5 pCi/L). The Big Bend and the Garlock-Big Pine fault system likely play an important role in stress distribution and fluid migration near the Carrizo Plain and more northern localities along the SAF; future research is required in order to confirm these interpretations.

Differences in soil CO_2 concentrations and $\delta^{13}C$ signatures at Parkfield between 2000 and 2016 illustrate temporal geochemical differences, which may prove a useful tool in earthquake prediction and understanding subsurface fluid movement. Future work should seek to monitor these shallow gases regularly both leading up to and following seismic events.

The large vertical array observed at SB-GR raises questions about the presence of small quantities of mantle CO_2 competing with other more depleted sources of CO_2 in the soil. To better understand the sources in this region it would be useful to perform dense analyses in the northen locked segment proximal to San Juan Baustista.

2.6 Acknowledgements

The authors would like to thank Shane Rooyakkers for his assistance in the field in November 2016. Thanks to John Erskine (GraniteRock), Scott Soares (California State Parks), Tony DeRose (DeRose Vineyards), Andy Snyder (U.S. Geological Survey), and Denis Kearns (California Bureau of Land Management) for their permission to access their lands so that we might study the fault. We thank Gregor Lucic and Linda Huynh from Picarro Inc. for their assistance with the instrument, especially during odd hours. This research was made possible with funding to Victoria Tweedie from NSERC, MAGNET, and the Department of Earth and Planetary Sciences, McGill University. This work was also support by NSERC Discovery, Accelerator, and Create grants to John Stix.

Figures

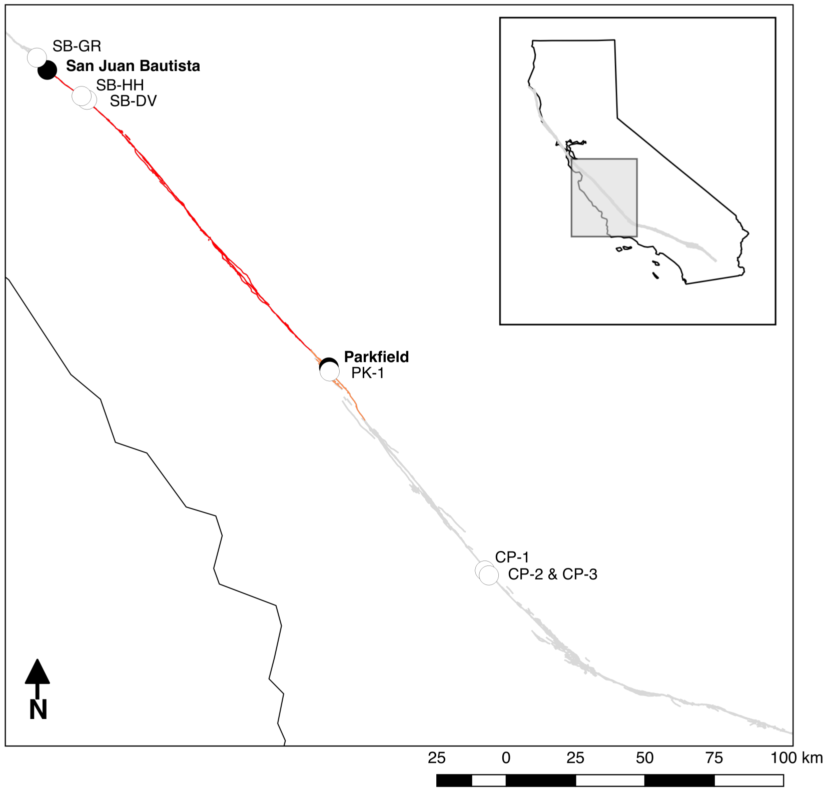

Figure 1: Localities of soil gas transects in California (white circles) and towns (black circles). Locked (grey), creeping (red), and transitional (orange) segments of the SAF are shown on the map.

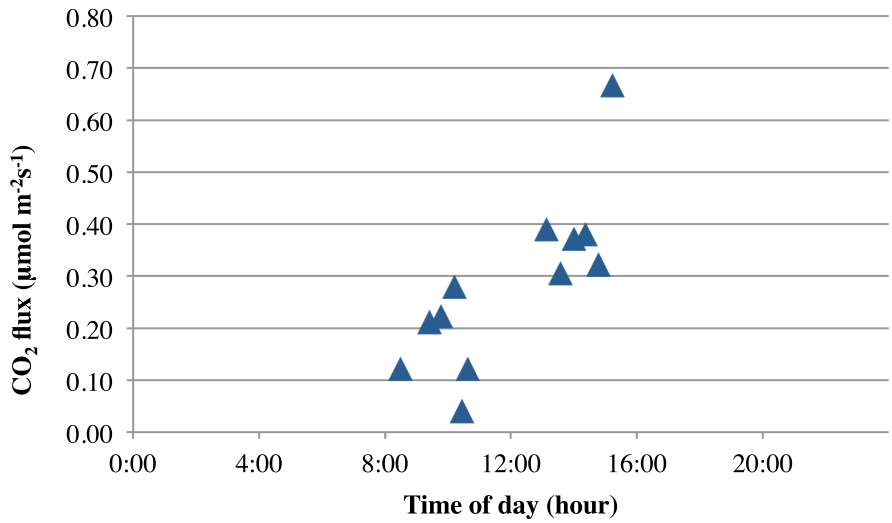

Figure 2: CO_2 flux measurements for transect CP-3 plotted against the time of day during which they were measured.

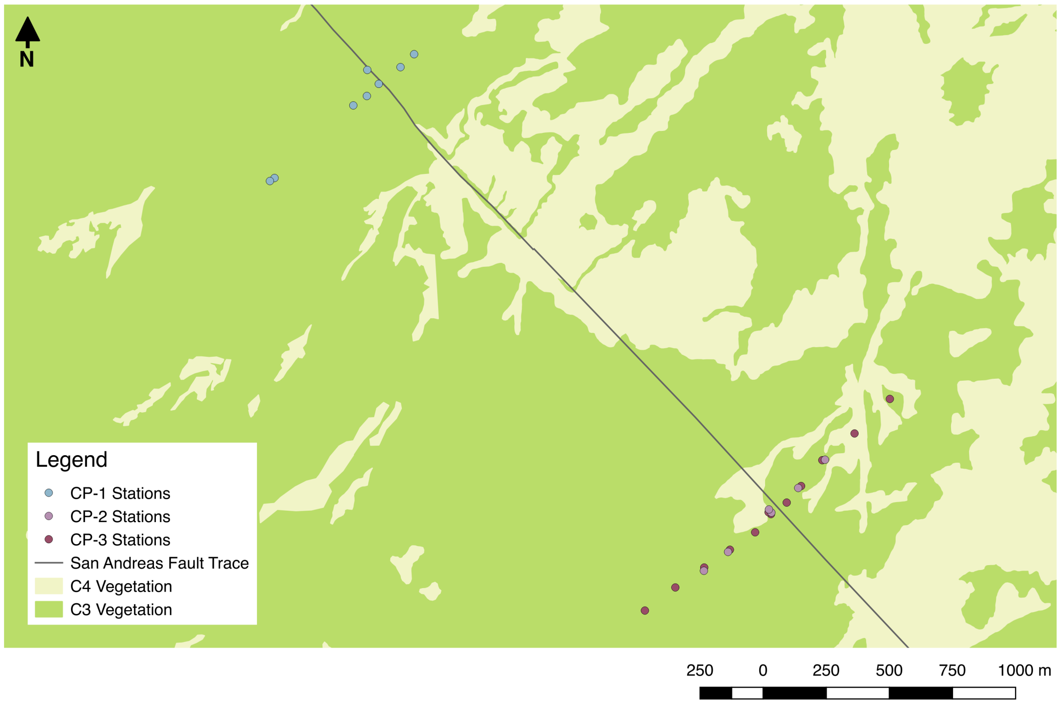

Figure 3: Spatial distribution of C3 and C4 vegetation in the Carrizo Plain near CP-1, CP-2, and CP-3 (data from Buck-Diaz and Evens, 2011).

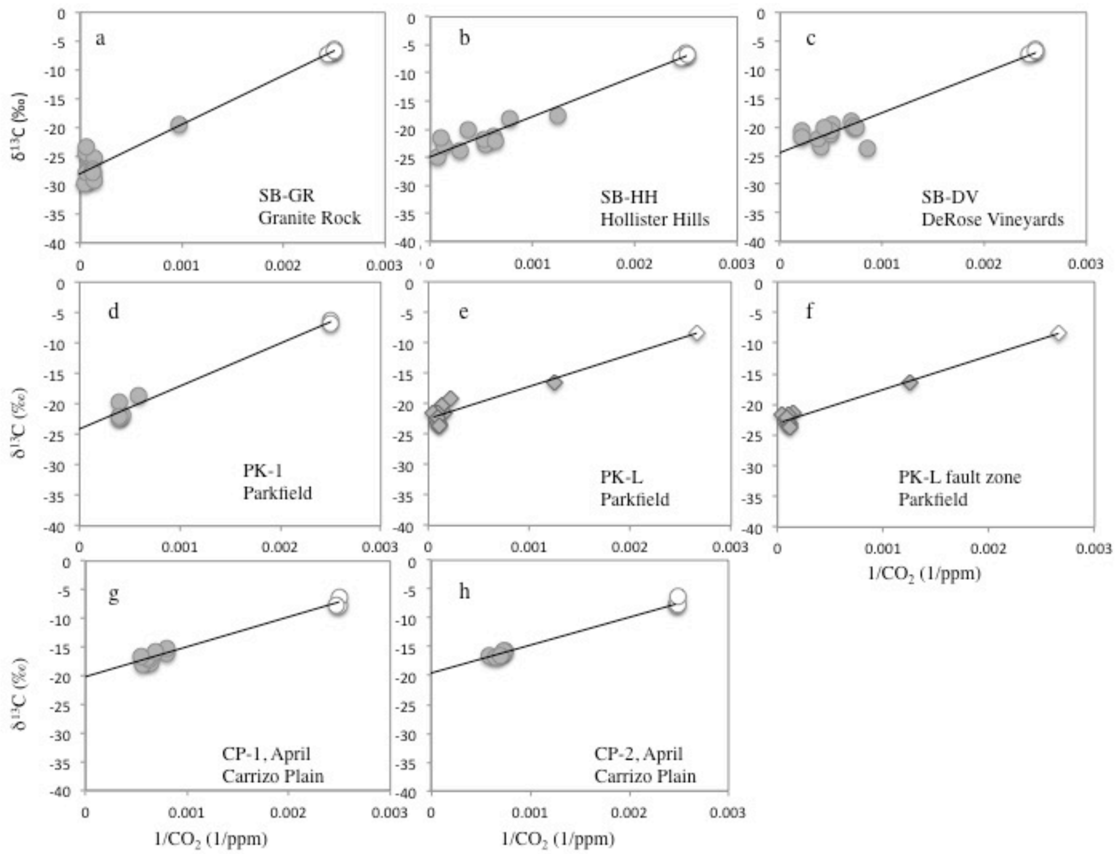

Figure 4: Keeling plot of atmospheric (white circle) and soil samples (grey circles) for transects (a) SB-GR, (b) SB-HH, (c) SB-DV, (d) PK-1, (e) PK-L, (f) PK-L fault zone, (g) CP-1, (h) CP-2. Linear intercepts for full transects are solid black. Diamonds denote atmospheric (white) and soil samples (grey) with data from Lewicki and Brantley (2000) and Lewicki et al. (2003).

Tables

Table 1: Soil and atmospheric gas measurements from soil transects

Station ID	Longitude	Latitude	Date	CO_2 (ppm)	$\delta^{13}C$ (‰)	error (±‰)	CH_4 (ppm)	H_2O (wt%)	Radon (pCi/L)^{L}	Radon (pCi/L)^{S}	CO_2 Flux Average (µmol m^{-2} s^{-1})	Standard Deviation (µmol m^{-2} s^{-1})	Date of CO_2 Flux Measurement	Time of CO_2 Flux Measurement
AT	**Atmospheric**													
SB-AT1	36.759	-121.407	23-Nov-17	409	-7.18	1.25	1.27	1.61						
SB-AT2	36.763	-121.403	23-Nov-17	399	-6.73	1.27	1.24	1.69						
SB-AT3	36.751	-121.382	23-Nov-17	399	-6.73	1.27	1.24	1.69						
SB-AT4	36.751	-121.382	23-Nov-17	400	-6.45	1.25	1.27	1.65						
PF-AT1	35.890	-120.427	28-Apr-16	399	-6.17	1.33	2.79	1.37						
PF-AT2	35.890	-120.427	28-Apr-16	399	-6.87	1.2	1.41	1.4						
CP-AT1	35.253	-119.816	24-Apr-16	400	-7.64	1.21	1.38	1.36						
CP-AT2	35.253	-119.816	24-Apr-16	400	-6.31	1.39	1.44	1.24						
CP-AT3	35.239	-119.797	23-Apr-16	405	-7.62	1.2	1.45	1.23						
CP-AT4	35.237	-119.801	25-Nov-16	406	-7.26	1.16	1.21	1.73						
CP	**Carrizo Plain**													
CP-1A	35.257	-119.810	24-Apr-16	1260	-16.13	0.57	0.47	1.08	303.70	347.92	0.99	0.03	24-Apr-16	10:24
CP-1B	35.257	-119.811	24-Apr-16	1246	-15.28	0.54	0.44	1.23	5215.80	1551.78	1.13	0.04	24-Apr-16	10:49
CP-1C	35.256	-119.812	24-Apr-16	1549	-17.62	0.45	0.59	1.28	311.70	344.19	1.27	0.05	24-Apr-16	11:13
CP-1D	35.257	-119.812	24-Apr-16	1757	-17.97	0.36	1.21	1.27	224.30	246.42	0.63	0.02	24-Apr-16	11:36
CP-1E	35.256	-119.812	24-Apr-16	1605	-17.14	0.4	0.36	1.38	423.50	486.98	0.80	0.05	24-Apr-16	14:01
CP-1F	35.255	-119.813	24-Apr-16	1646	-16.98	0.39	0.0026	1.35	345.20	389.74	1.02	0.04	24-Apr-16	0:00
CP-1G	35.253	-119.816	24-Apr-16	1440	-15.89	0.43	0.78	1.61						
CP-1H	35.253	-119.816	24-Apr-16	1802	-16.54	0.36	0.083	1.62						
CP-2A	35.242	-119.793	23-Apr-16	1718	-16.44	0.31	1.05	1.32	243.70	244.82	0.91	0.02	23-Apr-16	13:13
CP-2B	35.241	-119.794	23-Apr-16	1529	-16.91	0.42	1.3	1.35	331.50	372.43	0.61	0.02	23-Apr-16	13:39
CP-2C	35.240	-119.795	23-Apr-16	1362	-15.92	0.47	1.02	1.36	469.90	441.16	0.43	0.01	23-Apr-16	14:02
CP-2D	35.240	-119.795	23-Apr-16	1352	-15.72	0.53	0.83	1.32	445.50	459.27	1.23	0.06	23-Apr-16	14:29
CP-2E	35.238	-119.798	23-Apr-16	1358	-15.73	0.48	0.57	1.36	323.00	367.10	0.65	0.09	23-Apr-16	14:57
CP-2F	35.239	-119.797	23-Apr-16	1423	-16.53	0.5	1.13	1.4	232.90	886.85	0.90	0.03	23-Apr-16	0:00
CP-3A	35.240	-119.795	25-Nov-17	427	-9.9	1.34	1.32	1.37	529.50	497.64	0.67	0.03	25-Nov-17	10:12
CP-3B	35.240	-119.795	25-Nov-17	482	-12.59	1.19	1.44	1.23	269.40	526.14	0.28	0.04	26-Nov-17	14:47

CP-3C	35.241	-119.794	25-Nov-17	477	-11.45	0.97	1.37	1.13	375.30	391.61	0.32	0.01	25-Nov-17	14:22
CP-3D	35.241	-119.794	25-Nov-17	497	-10.48	0.81	1.43	1.16	271.40	360.44	0.38	0.02	25-Nov-17	14:00
CP-3E	35.242	-119.793	25-Nov-17	491	-11.7	0.85	1.42	1.06	336.70	485.11	0.37	0.04	25-Nov-17	13:35
CP-3F	35.243	-119.791	25-Nov-17	492	-9.68	0.81	1.48	1.08	266.00	355.64	0.31	0.01	25-Nov-17	13:08
CP-3G	35.244	-119.790	25-Nov-17	457	-10.06	1.11	1.45	1.18	445.90	479.52	0.39	0.01	25-Nov-17	10:27
CP-3H	35.240	-119.796	25-Nov-17	477	-11.68	1.01	1.57	1.09	421.70	466.73	0.04	0.02	26-Nov-17	10:38
CP-3I	35.243	-119.797	25-Nov-17	454	-11.04	1.19	1.57	1.43	378.80	480.59	0.12	0.02	26-Nov-17	8:30
CP-3J	35.238	-119.798	25-Nov-17	518	-10.7	1.22	1.65	1.52	287.40	338.33	0.12	0.04	26-Nov-17	9:25
CP-3K	35.238	-119.799	25-Nov-17	522	-11.11	1.05	1.71	1.45	235.10	237.10	0.21	0.03	26-Nov-17	9:47
CP-3L	35.237	-119.801	25-Nov-17	432	-9.28	1.11	1.71	1.2	282.40	358.31	0.22	0.07	26-Nov-17	0:00
PK	**Parkfield**													
PK-1A	35.888	-120.429	28-Apr-16	3920	-21.72	0.3	0.87	1.18	10108.40[D]	2611.80[D]	0.96	0.06	28-Apr-16	9:36
PK-1B	35.889	-120.429	28-Apr-16	3577	-22.26	0.26	0.87	1.3	62.10	52.21	0.71	0.06	28-Apr-16	10:25
PK-1C	35.889	-120.428	28-Apr-16	1695	-18.68	0.39	1.43	1.49	101.90	124.94	0.91	0.07	28-Apr-16	10:51
PK-1D	35.889	-120.428	28-Apr-16	2315	-21.83	0.3	0.5	1.54	9.90	23.18	1.13	0.06	28-Apr-16	11:15
PK-1E	35.889	-120.428	28-Apr-16	3182	-19.57	0.29	1.11	1.36	505.70	173.69	1.20	0.04	28-Apr-16	11:38
PK-1F	35.890	-120.427	28-Apr-16	2489	-21.98	0.3	1.07	1.5	251.30	266.40	1.37	0.15	28-Apr-16	12:00
SB	**San Benito County**													
SB-GRA	36.880	-121.586	21-Nov-17	14180	-29.09	0.47	1.51	0.74						
SB-GRB	36.880	-121.585	21-Nov-17	16253	-24.45	0.48	1.48	0.91						
SB GRC	36.879	-121.586	21-Nov-17	10530	-26.91	0.44	1.43	0.92						
SB-GRD	36.879	-121.587	21-Nov-17	11545	-27.46	0.44	1.31	1.15						
SB-GRE	36.879	-121.588	21-Nov-17	8200	-27.5	0.53	1.33	1.03						
SB-GRF	36.881	-121.583	21-Nov-17	25220	-29.72	0.47	1.53	0.89						
SB-GRG	36.881	-121.583	21-Nov-17	7282	-25.34	0.38	1.38	1.09						
SB-GRG2	36.881	-121.583	21-Nov-17	15746	-23.37	0.52	1.45	1.13						
SB-GRH	36.881	-121.583	21-Nov-17	**1032**	-19.39	0.53	1.24	1.78						
SB-GRI	36.881	-121.583	21-Nov-17	7976	-27.7	0.41	1.06	1.77						
SB-GRJ	36.882	-121.582	21-Nov-17	16235	-27.73	-0.39	1.17	1.77						
SB-GRK	36.883	-121.581	21-Nov-17	7074	-29.2	-0.46	1.19	1.84						
SB-GRL	36.883	-121.580	21-Nov-17	8066	-27.21	0.49	1.14	1.36						
SB-GRM	36.884	-121.579	21-Nov-17	7755	-27.67	0.44	1.23	1.97						
SB-HHA	36.761	-121.405	23-Nov-17	13180	-24.88	0.48	1.41	1.22						
SB-HHB	36.761	-121.405	23-Nov-17	3412	-23.85	0.38	1.15	1.26						
SB-HHC	36.761	-121.405	23-Nov-17	7941	-23.11	0.41	1.34	1.11						
SB-HHD	36.761	-121.405	23-Nov-17	9717	-21.62	0.32	1.28	1.23						
SB-HHE	36.760	-121.406	23-Nov-17	2748	-20.15	0.43	1.16	1.44						
SB-HHF	36.759	-121.407	23-Nov-17	1622	-21.16	0.33	1.18	1.65						
SB-HHG	36.762	-121.404	23-Nov-17	1294	-18.25	0.45	1.16	1.74						

SB-HHH	36.762	-121.404	23-Nov-17	1864	-22.81	0.52	1.15	1.57
SB-HHI	36.763	-121.404	23-Nov-17	808	-17.45	0.59	1.24	1.62
SB-HHJ	36.763	-121.403	23-Nov-17	1906	-21.88	0.57	1.08	1.58
SB-HHK	36.763	-121.403	23-Nov-17	1561	-22.2	0.83	1.21	1.63
SB-DVA	36.746	-121.390	22-Nov-17	2538	-23.44	0.43	1.19	1.61
SB-DVB	36.747	-121.389	22-Nov-17	4717	-20.77	0.57	1.12	1.57
SB-DVC	36.748	-121.387	22-Nov-17	1950	-19.59	-0.62	1.29	1.61
SB-DVD	36.748	-121.386	22-Nov-17	1441	-19.11	0.69	1.44	1.69
SB-DVE	36.749	-121.385	22-Nov-17	2670	-22.05	0.52	1.47	1.76
SB-DVF	36.749	-121.384	22-Nov-17	4581	-21.7	0.51	1.07	1.65
SB-DVG	36.749	-121.384	22-Nov-17	1999	-21.2	0.29	1.13	1.89
SB-DVH	36.749	-121.384	22-Nov-17	1169	-23.8	0.56	1.23	1.57
SB-DVI	36.749	-121.385	23-Nov-17	2025	-20.73	0.76	1.41	1.48
SB-DVJ	36.750	-121.383	23-Nov-17	2339	-20.05	0.59	1.33	1.43
SB-DVK	36.750	-121.383	23-Nov-17	1405	-19.79	0.56	1.15	1.44
SB-DVL	36.751	-121.382	23-Nov-17	1347	-19.98	0.45	1.06	1.69

[L] Radon was measured with long-term electrets paired with a L chamber

[S] Radon was measured with short-term electrets paired with a M chamber

[D] Radon electret was dirty when removed from the soil and measurements are not reliable

Table 2: Well gas measurements in Parkfield and San Benito County

Well ID	Region Group	Longitude	Latitude	Sample Depth (m)	Date	CO_2 (ppm)	$\delta^{13}C$ (‰)	error (±‰)	H_2O (wt%)
WFF	Parkfield	-120.514	35.932	20	27-Apr-16	1615	-23.01	0.45	1.09
WHV[d]	Parkfield	-120.427	35.889	10	27-Apr-16	835	-17.43	2.56	0.75
WHV	Parkfield	-120.427	35.889	10	27-Apr-16	824	-18.72	0.67	1.17
WGH *	Parkfield	-120.434	35.921	20	27-Apr-16	11805	-26.71	0.33	0.87
CR-2	San Benito County	-121.587	36.883	3	20-Apr-16	578	-14.11	0.79	1.44
DW-2	San Benito County	-121.607	36.893	10	20-Apr-16	2277	-25.06	0.23	1.43
DW-11 *	San Benito County	-121.605	36.891	30	20-Apr-16	182353	-24.74	0.39	0.75
DW-7	San Benito County	-121.627	36.906	4	20-Apr-16	2027	-33.48	0.72	1.34
CH-1	San Benito County	-121.607	36.903	6	20-Apr-16	759	-14.99	0.74	1.51
DW-3	San Benito County	-121.622	36.894	10	21-Apr-16	6467	-27.53	0.34	0.78
DW-3	San Benito County	-121.622	36.894	30	21-Apr-16	22267	-30.00	0.30	2.88
DW-3	San Benito County	-121.622	36.894	50	21-Apr-16	37590	-34.22	0.31	0.69
UNAVCO-1	San Benito County	-121.622	36.894	10	21-Apr-16	1932	-29.77	0.27	1.76
UNAVCO-1	San Benito County	-121.622	36.894	30	21-Apr-16	1305	-23.34	0.39	1.78

[d] sample was diluted prior to measurements

Table 3: Literature C3 vegetation $\delta^{13}C$ signatures from areas of comparable annual precipitation and elevation

Region Group	Source*	Sampling Year	Altitude (m.a.s.l.)	Annual Precipitation (mm)	Plant $\delta^{13}C$
San Benito County (SB)					
	Cerling & Harris (1999)	1982	150	380	-27.7
	Cerling & Harris (1999)	1998	150	380	-26.5
	Cerling & Harris (1999)	1983	50	380	-27.8 [a]
	Hartman & Danin (2010)	2007	346	375	-26.9
	Hartman & Danin (2010)	2007	347	356	-27.3
	Kloeppel et al. (1998)		556	390	-27.5
	Miller et al. (2001)	1996	360	400	-26.5
	Miller et al. (2001)	1996	380	390	-26.6
	Miller et al. (2001)	1996	400	370	-25.5 [b]
Parkfield (PK)					
	Cerling & Harris (1999)	1984	150	330	-25.4
	Hartman & Danin (2010)	2007	269	314	-26.3 [a]
	Hartman & Danin (2010)	2007	245	314	-26.3 [a]
	Miller et al. (2001)	1996	420	350	-26.3
	Miller et al. (2001)	1996	440	320	-25.1
	Miller et al. (2001)	1996	460	300	-25.3
	Miller et al. (2001)	1996	480	300	-24.6 [b]
	Schulze et al. (1998)	1993	355	342	-26.0
	Schulze et al. (1998)	1993	470	329	-25.9
	Schulze et al. (1998)	1993	560	310	-25.2
Carrizo Plain (CP)					
	Cerling & Harris (1999)	1995	425	200	-25.4
	Escudero et al. (2008)	2002	789	241	-26.7 [a]
	Miller et al. (2001)	1996	580	230	-25.3
	Miller et al. (2001)	1996	600	200	-24.9
	Schulze et al. (1998)	1993	780	216	-25.5
	Swap et al. (2004)	2002	940	230	-23.2 [b]

* studies are not from the same location as the region group, but they are in comparable environments within 2 " of annual precipitation and less than 1000 m elevation

[a] lowest $\delta^{13}C$ signature for region group

[b] highest $\delta^{13}C$ signature for region group

Table 4: Keeling plot intercepts and mantle contribution ranges of each full transect

Transect	Keeling Y-Intercept		Mantle End-Member		Biogenic End-Member		% Mantle (p_M)			Mantle CO_2 Flux (μmol $m^{-2}s^{-1}$)		
	$\delta^{13}C$ (‰)	R^2	Min. $\delta^{13}C$	Max. $\delta^{13}C$	Min. $\delta^{13}C$ [A]	Max. $d^{13}C$ [B]	Highest[A]	Lowest[B]	Error	Min.	Max.	Error
SB-GR	-24.08	0.97	-9.00	-4.00	-29.99	-24.50	0.00	0.00	11.68			
SB-HH	-24.46	0.96	-9.00	-4.00	-29.99	-24.50	24.21	0.00	0.84			
SB-DV	-27.98	0.93	-9.00	-4.00	-29.99	-24.50	26.35	0.22	8.83			
PK-1	-24.08	0.97	-9.00	-4.00	-25.88	-23.60	10.64	0.00	8.29	0.00	0.15	0.12
PK-L	-22.45	0.95	-9.00	-4.00	-25.88	-23.60	20.31	5.88				
PK-L FZ	-23.06	0.98	-9.00	-4.00	-25.88	-23.60	16.68	2.76				
CP-1	-20.16	0.98	-9.00	-4.00	-26.28	-22.20	35.43	11.24	12.69	0.07	0.45	0.11
CP-2	-19.68	0.99	-9.00	-4.00	-26.28	-21.80	38.16	11.66	10.49	0.05	0.47	0.13

[A] Autotrophic isotopic fractionation used in this calculation was +1.7 ‰
[B] Autotrophic isotopic fractionation used in this calculation was +4.0 ‰
PK-L Soil gas data from Lewicki and Brantley (2000) and Lewicki et al. (2003)
FZ fault zone

Chapter Three: Major conclusions and suggestions for future work

The most significant points of this thesis are as follows:

1. High precision CO_2 concentrations and $\delta^{13}C$ signatures of gases are obtained from CRDS measurements. However, large errors in $\delta^{13}C$ measurements arise at low CO_2 concentrations as was observed along transect CP-3. Future work should continue to measure gas samples with CO_2 concentrations between 1000 and 2000 ppm.
2. Low contributions of mantle CO_2 to the shallow SAF can be detected by careful analyses consisting of high precision measurements by CRDS and the use of Keeling plots. Keeling plots can provide representative $\delta^{13}C$ signature for a region. When combined with known end-member $\delta^{13}C$ signatures (e.g., biogenic and mantle), we are able to determine the contribution of these end-members to the region, even when one is present in small quantities.
3. CO_2 mixing proportions and fluxes along the SAF reveal increasing mantle enrichment from north (0 %, 0 μmol m^{-2}s^{-1}) to south (38.16 %, 0.47 μmol m^{-2}s^{-1}). This trend is unexpected as it reveals a relatively high quantity of mantle fluid in the locked Carrizo Plain relative to regions that are known for being more permeable. This finding highlights a lack of understanding of subsurface processes occurring near the Carrizo Plain such as the role of the Big Bend and the Garlock-Big Pine fault zones on fluids in the SAF system.
4. *The* $\delta^{13}C$ variation, as demonstrated by a large vertical array in transect SB-GR, may be reflective of multiple sources of CO_2, including mantle CO_2 in small quantities, despite depleted $\delta^{13}C$ signatures. Additional analyses of the northern locked segment proximal to San Juan Bautista are required in order to better understand fluid origins and migration in the shallow fault system in this region.

5. Differences in soil CO_2 concentrations and $\delta^{13}C$ signatures at Parkfield between 2000 (797 to 20900 ppm, -23.06 ‰; from Lewicki and Brantley, 2000 and Lewicki et al., 2003) and 2016 (1695 to 3920 ppm, -24.08 ‰; this study) may illustrate temporal geochemical differences in the fault system. Future annual or semi-annual monitoring leading up to and following an earthquake may provide insight into fluid migration prior and following a seismic event in the shallow fault system.

Contribution to Knowledge

This thesis presents a spatial investigation of soil carbon isotopes performed over two separate two-week intervals in April and November 2016. High precision geochemical analyses of CO_2 gas along the SAF by CRDS using Keeling plots provide insight into CO_2 sources in the shallow fault system in San Benito County, Parkfield, and the Carrizo Plain. Evidence for mantle CO_2 in the shallow fault system presented in this work is the first of its kind, revealing that deep fluids migrate to, and can be detected at, shallow depths. The discovery of a mantle contribution in the Carrizo Plain, relative to both Parkfield and San Benito County, illustrates the importance of understanding the processes influencing this area, especially since it is overdue for an earthquake.

Topics for Future Research

The findings from this work provide a starting point for a variety of future research concerning the SAF and mantle fluids. Future studies should seek to better characterize variation in mantle contributions across the fault in order to understand differences in contributions (1) proximal and distal to the fault and (2) between the North American and Pacific plates. Work of this sort will provide a better understanding of shallow fluid origin and migration in the fault system and aid in understanding how different geologic units influence mantle fluids migration at different localities along the SAF. This will help to establish whether mantle fluid in the shallow fault is controlled by regional processes or whether more local phenomena have a greater influence on fluid migration.

Continuous geochemical monitoring of fluids (e.g., gases or liquids) prior to, during, and following earthquake activity will provide insight into fluid migration leading up to and following these events. This will allow us to understand whether CO_2 concentration or $\delta^{13}C$ signatures change as a result of gas flux to the system during dilation by seismic waves.

The Carrizo Plain is a region of interest, and as a result it is important to understand the role that the Big Bend section and the Garlock-Big Pine fault systems play in subsurface fluid migration and distribution in this area.

References

Becken, M., O. Ritter, S. K. Park, P. A. Bedrosian, U. Weckmann, and M. Weber (2008), A deep crustal fluid channel into the San Andreas Fault system near Parkfield, California, *Geophysical Journal International* 173(2), 718-732.

Bedrosian, P. A., M. J. Unsworth, G. D. Egbert, and C. H. Thurber (2004), Geophysical images of the creeping segment of the San Andreas fault: implications for the role of crustal fluids in the earthquake process, *Tectonophysics* 385(1), 137-158.

Bowling, D. R., D. E. Pataki, and J. T. Randerson (2008), Carbon isotopes in terrestrial ecosystem pools and CO_2 fluxes, *New Phytologist* 178(1), 24-40.

Buck-Diaz, J., and J. Evens (2011), Carrizo Plain National Monument vegetation classification and mapping project, *Report submitted to the Bureau of Land Management, California Native Plant Society, Sacramento, CA*.

Byerlee, J. (1990) Friction, overpressure and fault normal compression, *Geophysical Research Letters* 17(12), 2109-2112.

Byerlee, J. (1992), The change in orientation of subsidiary shears near faults containing pore fluid under high pressure, *Tectonophysics* 211(1), 295-303.

Cerling, T. E., and J. M., Harris (1999) Carbon isotope fractionation between diet and bioapatite in ungulate mammals and implications for ecological and paleoecological studies, *Oecologia*, *120*(3), 347-363.

Escudero, A., S., Mediavilla, and H., Heilmeier (2008) Leaf longevity and drought: avoidance of the costs and risks of early leaf abscission as inferred from the leaf carbon isotopic composition, *Functional Plant Biology*, *35*(8), 705-713.

Evans, T. J. (2013), Helium and carbon isotope systematics in groundwaters along the southern San Andreas fault system, *UC San Diego Electronic Theses and Dissertations*.

Hartman, G., and A., Danin (2010), Isotopic values of plants in relation to water availability in the Eastern Mediterranean region, *Oecologia* 162(4), 837-852.

Hauri, E., K. Grönvold, N. Öskarsson, and D. McKenzie (2002), Abundance of carbon in the Icelandic mantle: constraints from melt inclusions, *AGU Spring Meeting Abstracts*, V51D-03.

Irwin, W. P., and I. Barnes (1975), Effect of geologic structure and metamorphic fluids on seismic behavior of the San Andreas fault system in central and northern California, *Geology* 3(12), 713-716.

Jennings C. W. and R. G Strand (1969) Geologic map of California: Los Angeles sheet, California Division of Mines and Geology.

Kloeppel, B. D., S. T., Gower, I. W., Treichel, and S., Kharuk (1998) Foliar carbon isotope discrimination in Larix species and sympatric evergreen conifers: a global comparison. *Oecologia*, *114*(2), 153-159.

Kohn, M. J. (2010), Carbon isotope compositions of terrestrial C3 plants as indicators of (paleo) ecology and (paleo) climate, *Proceedings of the National Academy of Sciences* 107(46), 19691-19695.

Kulongoski, J. T., D. R. Hilton, P. H. Barry, B. K. Esser, D. Hillegonds, and K. Belitz (2013), Volatile fluxes through the Big Bend section of the San Andreas Fault, California: helium and carbon-dioxide systematics, *Chemical Geology*, *339*, 92-102.

Laznicka, P. (2010), Giant metallic deposits, London: Springer, 496.

Lewicki, J. L., and S. L. Brantley (2000), CO_2 degassing along the San Andreas fault, Parkfield, California, *Geophysical Research Letters* 27(1), 5-8.

Lewicki, J. L., W. C. Evans, G. E. Hilley, M. L. Sorey, J. D. Rogie, and S. L. Brantley (2003), Shallow soil CO_2 flow along the San Andreas and Calaveras faults, California, *Journal of Geophysical Research: Solid Earth*, *108*(B4).

LI-COR Biosciences Inc. (2012), LI-8100A Automated Soil CO2 Flux System & LI-8150 Multiplexer Instruction Manual, pp. 4-4, Lincoln, Nebraska.

Lucic, G., J. Stix, and B. Wing (2015), Structural controls on the emission of magmatic carbon dioxide gas, Long Valley Caldera, USA, *Journal of Geophysical Research: Solid Earth* 120(4), 2262-2278.

Malowany, K., J. Stix, A. Van Pelt, and G. Lucic (2015), H_2S interference on CO_2 isotopic measurements using a Picarro G1101-i cavity ring-down spectrometer, *Atmospheric Measurement Techniques* 8(10), 4075-4082.

O'Leary, M. H. (1988), Carbon isotopes in photosynthesis, *Bioscience* 38(5), 328-336.

Oldow, J. S., and P. H. Cashman (2009), Late Cenozoic Structure and Evolution of the Great Basin-Sierra Nevada, *Geological Society of America*, 362-363.

Petraki, E., D., Niolopoulos, D., Panagiotaras, D., Cantzos, P., Yannakopoulos, C., Nomicos, and J., Stonham (2015) Radon-222: a potential short-term earthquake precursor, *Journal of Earth Science & Climatic Change*, 6(6), 1-11.

Pineau, F., and M. Javoy (1983), Carbon isotopes and concentrations in mid-oceanic ridge basalts, *Earth and Planetary Science Letters* 62(2), 239-257.

Rice, J. R. (1992), Fault stress states, pore pressure distributions, and the weakness of the San Andreas fault, *International Geophysics* 51, 475-503.

Ross, D. C. (1970), Quartz gabbro and anorthositic gabbro: Markers of offset along the San Andreas fault in the California Coast Ranges, *Geological Society of America Bulletin* 81(12), 3647-3662.

San Benito County (1994), Environmental resources and constraints inventory, San Benito County Board of Supervisors, 72.

San Benito County (2010), General Plan: Chapter 11- Safety, San Benito County Board of Supervisors, 11-20.

Schulze, E. D., R. J., Williams, G. D. Farquhar, W., Schulze, J., Langridge, J. M., Miller, and B. H., Walker (1998) Carbon and nitrogen isotope discrimination and nitrogen nutrition of trees along a rainfall gradient in northern Australia *Functional Plant Biology*, *25*(4), 413-425.

Smith, B. N., and S. Epstein (1971), Two categories of $^{13}C/^{12}C$ ratios for higher plants, *Plant Physiology* 47(3), 380-384.

Sorey, M. L., W. C. Evans, B. M. Kennedy, C. D. Farrar, L. J. Hainsworth, and B. Hausback (1998), Carbon dioxide and helium emissions from a reservoir of magmatic gas beneath Mammoth Mountain, California, *Journal of Geophysical Research: Solid Earth*, *103*(B7), 15303-15323.

Swap, R. J., J. N., Aranibar, P. R., Dowty, W. P., Gilhooly, and S. A., Macko (2004) Natural abundance of ^{13}C and ^{15}N in C3 and C4 vegetation of southern Africa: patterns and implications, *Global Change Biology*, *10*(3), 350-358.

Thordsen, J. J., W. C. Evans, and Y. K. Kharaka (2010), Geochemistry of formation fluids from the SAFOD wells, Parkfield, California, *EOS Transactions AGU 91 (52). Fall Meet. Suppl.*, Abstract T41A-2098.

Titus, S. J., C. DeMets, and B. Tikoff (2006), Thirty-five-year creep rates for the creeping segment of the San Andreas fault and the effects of the 2004 Parkfield earthquake: Constraints from alignment arrays, continuous global positioning system, and creepmeters, *Bulletin of the Seismological Society of America* 96(4B), S250-S268.

Tu, K. P., and T. E. Dawson (2003), Variation in 13C abundance in respiration among ecosystem components: implications for flux partitioning, *AGU Fall Meeting Abstracts*, B31E-0351.

Unsworth, M. J., P. E. Malin, G. D. Egbert, and J. R. Booker (1997), Internal structure of the San Andreas fault at Parkfield, California, *Geology*, *25*(4), 359-362.

Unsworth, M. J., G. D. Egbert, and J. Booker (1999), High-resolution electromagnetic imaging of the San Andreas fault in central California, *Journal of Geophysical Research: Solid Earth* 104(B1), 1131-1150.

Unsworth, M. J., P. Bedrosian, M. Eisel, G. D. Egbert, & W. Siripunvaraporn (2000), Along strike variations in the electrical structure of the San Andreas Fault at Parkfield, California, *Geophysical Research Letters*, *27*(18), 3021-3024.

U.S. Geological Survey (2008), The ShakeOut scenario, *U.S. Geological Survey Open File report,* 2008-1150.

Wallace R.E. (1990), The San Andreas Fault System, California, *U.S. Geological Survey Professional Paper* 1515, 283.

Wiersberg, T., and J. Erzinger (2007), A helium isotope cross-section study through the San Andreas Fault at seismogenic depths, *Geochemistry, Geophysics, Geosystems* 8, Q01002, doi:10.1029/2006GC001388.